

Physics-Driven Autoregressive State Space Models for Medical Image Reconstruction

Bilal Kabas, Fuat Arslan, Valiyeh A. Nezhad, Saban Ozturk, Emine U. Saritas, and Tolga Çukur*

Abstract—Medical image reconstruction from under-sampled acquisitions is an ill-posed problem that involves inversion of the imaging operator linking measurement and image domains. In recent years, physics-driven (PD) models have gained prominence in learning-based reconstruction given their enhanced balance between efficiency and performance. For reconstruction, PD models cascade data-consistency modules that enforce fidelity to acquired data based on the imaging operator, with network modules that process feature maps to alleviate image artifacts due to undersampling. Success in artifact suppression inevitably depends on the ability of the network modules to tease apart artifacts from underlying tissue structures, both of which can manifest contextual relations over broad spatial scales. Convolutional modules that excel at capturing local correlations are relatively insensitive to non-local context. While transformers promise elevated sensitivity to non-local context, practical implementations often suffer from a suboptimal trade-off between local and non-local sensitivity due to intrinsic model complexity. Here, we introduce a novel physics-driven autoregressive state space model (MambaRoll) for enhanced fidelity in medical image reconstruction. In each cascade of an unrolled architecture, MambaRoll employs an autoregressive framework based on physics-driven state space modules (PSSM), where PSSMs efficiently aggregate contextual features at a given spatial scale while maintaining fidelity to acquired data, and autoregressive prediction of next-scale feature maps from earlier spatial scales enhance capture of multi-scale contextual features. Demonstrations on accelerated MRI and sparse-view CT reconstructions indicate that MambaRoll outperforms state-of-the-art PD methods based on convolutional, transformer and conventional SSM modules.

Index Terms—medical image reconstruction, undersampling, state space, autoregressive, physics-driven

I. INTRODUCTION

In many tomographic modalities, tissue structure in image domain is subjected to spatial encoding prior to acquisition, resulting in raw data to reside in a separate measurement domain (e.g., k-space in MRI, projection domain in CT) [1]. Higher spatial resolution can be sought by increasing the number of unique encodings collected in this measurement

domain, albeit this results in prolonged scan times and patient discomfort. A mainstream solution to improve scan efficiency relies on undersampled acquisitions, e.g., collecting a subset of k-space points in MRI, or a subset of projection views in CT [2]. Note, however, that reconstructing images from raw data is an ill-posed problem that requires inversion of the imaging operator linking measurement and image domains. Unfortunately, traditional reconstruction methods can perform suboptimally, often leaving structured aliasing artifacts and elevated noise in reconstructed images [3], [4]. Therefore, there is a dire need for enhanced reconstruction methods that push the envelope of diagnostic quality for medical images recovered from undersampled acquisitions.

Learning-based methods have made notable progress in medical image reconstruction over the recent years. A first group of methods focus on building image priors decoupled from the influences of the imaging operator [5]–[10]. In this group, data-driven methods build conditional priors operationalized as network models that map images linearly recovered from undersampled acquisitions to ground-truth images derived from fully-sampled data [7], [11]. While this purely data-driven approach benefits from task-specific feature extraction innate to deep learning, ignoring the imaging operator that was prescribed to acquire data can cause suboptimal performance and poor generalization [12]. Meanwhile, generative methods typically build unconditional priors where network models learn to synthesize high-quality medical images [13]–[18]. To enable reconstruction via such unconditional priors, inference procedures are required that optimize a combined objective including regularization based on the image prior and consistency to acquired data based on the imaging operator [19], [20]. As such, despite their promise in generalization and flexibility, generative methods might lower practicality as they require extended inference times [21].

In the literature, physics-driven (PD) methods come forth given their favorable balance between efficiency and performance in medical image reconstruction [22]. PD methods build conditional priors to map undersampled to fully-sampled data; but instead of relying solely on data-driven processing, they adopt unrolled architectures that interleave network modules to suppress artifacts in reconstructions, with data-consistency modules that enforce fidelity to acquired data based on the imaging operator [23]–[27]. Naturally, the success of an unrolled architecture in alleviating undersampling-related artifacts depends on the ability of the network modules to separate artifacts from underlying tissue structure, both of

This study was supported in part by TUBA GEBIP 2015 and BAGEP 2017 fellowships, and by a TUBITAK 1001 Grant 121E488 awarded to T. Çukur (Corresponding author: Tolga Çukur, cukur@ee.bilkent.edu.tr).

B. Kabas, F. Arslan, V.A. Nezhad, S. Ozturk, E.U. Saritas, and T. Çukur are with the Dept. of Electrical-Electronics Engineering and National Magnetic Resonance Research Center (UMRAM), Bilkent University, Ankara, Turkey, 06800. E.U. Saritas and T. Çukur are also with the Neuroscience Graduate Program Bilkent University, Ankara, Turkey, 06800.

which can show contextual relations over broad spatial scales [28]. Earlier convolutional modules are adept at capturing local correlations, albeit they suffer from insensitivity to non-local context [5], [29]–[31]. While transformer modules have been poised to improve sensitivity to long-range correlations, the intrinsic complexity of self-attention layers introduce heavy computational burden, restricting spatial precision and training efficacy in practical implementations [32]–[41].

State space models (SSM) are emerging as a promising alternative to convolutional and transformer backbones for imaging tasks [42]. SSMs scan through pixels in an image to raster them into a one-dimensional sequence, and perform recurrent modeling via a dynamical system formulation so as to capture relationships between sequence elements. This approach promises enhanced sensitivity to long-range context over convolutional backbones, and a refined trade-off between contextual sensitivity and local precision compared to transformers [43], [44]. Accordingly, few recent studies have adopted SSM-based network modules as part of purely data-driven architectures in medical image reconstruction [45], [46]. Note that data-driven SSM models that neglect the imaging operator may perform suboptimally as they inherently share the limitations of data-driven architectures in generalization. A recent study has instead proposed an unrolled architecture based on conventional SSM modules that process feature maps at a single spatial scale [47]. While this physics-driven method can offer improved performance, conventional SSM modules suffer from limited sensitivity to contextual interactions between relatively distant pixels that are connected through broad paths across the sequence [42]. In turn, this can restrict success in aggregation of contextual features evident across diverse spatial scales in medical images [48].

Here, we introduce a novel physics-based autoregressive state space model, MambaRoll, for enhanced fidelity in medical image reconstruction (Fig. 1). As a physics-driven model, MambaRoll is based on an unrolled architecture that interleaves network and data-consistency modules. Yet, unlike previous methods, each cascade of MambaRoll recovers high-resolution feature maps progressively across multiple spatial scales by leveraging autoregressive prediction of next-scale feature maps from earlier scales. This autoregressive framework serves to facilitate image recovery by improving capture of multi-scale contextual features in medical images. At a given scale, recovery is performed by novel physics-driven state space modules (PSSM) that efficiently aggregate contextual features while maintaining consistency to acquired data. Unlike conventional SSM modules, PSSM comprises a convolutional encoder to map high-resolution feature maps to the desired scale, a shuffled SSM block to capture context across feature maps, a convolutional decoder to recollect high-resolution feature maps, and a residual data-consistency block to enforce fidelity to acquired data. Comprehensive demonstrations on accelerated MRI and sparse-view CT reconstructions indicate that MambaRoll significantly outperforms state-of-the-art PD methods based on convolutional, transformer and conventional SSM modules. Code for MambaRoll is available at <https://github.com/icon-lab/MambaRoll>.

Contributions:

- To our knowledge, MambaRoll is the first physics-driven autoregressive state-space model for medical image reconstruction in the literature.
- In each cascade of its unrolled architecture, MambaRoll leverages autoregressive predictions of next-scale feature maps to aggregate contextual representations progressively across multiple spatial scales.
- Autoregressive predictions are enabled by a novel PSSM module that comprises encoder, shuffled SSM, decoder blocks followed by a residual data-consistency layer. PSSM serves to regularize feature maps for artifact mitigation at different scales while enforcing residual consistency to acquired data at the full scale.

II. RELATED WORK

A. Physics-Driven Models

Deep learning has empowered leaps in performance over traditional approaches for medical image reconstruction. Among learning-based methods, physics-driven (PD) models have emerged as a powerful approach that builds conditional image priors to map images linearly recovered from undersampled data to ground-truth images derived from fully-sampled data [22]. PD models perform reconstruction via a single forward pass through an unrolled architecture that embodies the imaging operator, so they offer a favorable balance between efficiency and performance [29]. Inevitably, however, the utility of a PD model in suppressing undersampling artifacts depends on the ability of the network modules in the unrolled architecture responsible for regularizing reconstructions. Note that tissue signals in medical images manifest significant correlations over short- to- long-range spatial distances, and hence aliasing artifacts that depend on the interaction between tissue structure and imaging operators can also manifest substantial spatial correlations [49]. During medical image reconstruction, expression of these contextual features is key to successful separation of artifacts from underlying tissue structure [34].

Earlier PD models have considered convolutional modules that use compact, shift-invariant filters to process feature maps [5], [29], [30], [50]. This locality bias improves efficiency and local precision, and convolutional PD models can offer high image quality in relatively less challenging tasks where separation of artifacts from tissue structure does not rely on long-range contextual features. Yet, they can suffer from limited performance in reconstruction tasks involving prominent, distributed patterns of artifacts. Later PD models have instead adopted transformer modules based on self-attention filters to address this issue [40], [51], [52]. Since self-attention is agnostic to spatial distance, transformer PD models can enhance sensitivity to long-range spatial context at the expense of elevated model complexity. However, the intrinsic complexity of transformers typically restricts their use to capture interactions among relatively crude image patches, compromising local precision [32]–[38]. Despite important attempts at alleviating this restriction, transformer modules

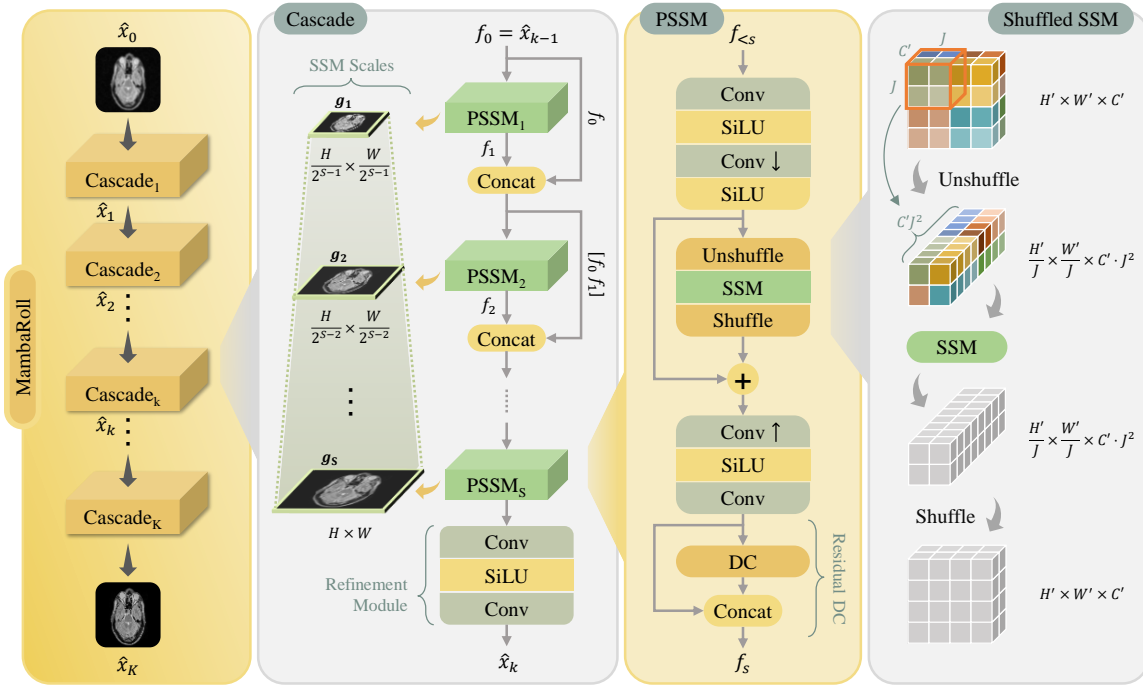


Fig. 1: MambaRoll is a novel physics-driven autoregressive state space model, which utilizes an unrolled architecture with K cascades to map a linear reconstruction of undersampled data \hat{x}_0 to the learning-based reconstruction \hat{x}_K . In each cascade, MambaRoll recovers contextualized feature maps at high spatial resolution g_S progressively across S spatial scales by leveraging autoregressive prediction of next-scale feature maps from earlier scales. At a given scale s , recovery is performed by a novel physics-driven state space module (PSSM) that efficiently aggregates contextual features while maintaining consistency to acquired data. PSSM comprises a convolutional encoder to map input feature maps $f_{<s}$ to the desired scale, a shuffled SSM block to capture context across feature maps efficiently, a convolutional decoder to recollect high-resolution feature maps, and a residual data-consistency block to enforce fidelity to acquired data. Following autoregressive predictions, a refinement module based on convolutional layers is used to enhance restoration of detailed texture.

face significant challenges in maintaining a balance between sensitivity to local versus global features [53], [54].

B. State-Space Models

SSMs have recently emerged as a powerful alternative to convolutional and transformer backbones given their ability to capture long-range contextual relations without compromising efficiency or local precision [43], [44], [55]. Inspired by the promise of SSMs in imaging tasks, here we introduce MambaRoll as a novel technique to recover medical images from undersampled acquisitions. To our knowledge, MambaRoll is the first physics-driven autoregressive SSM model for medical image reconstruction, and the first autoregressive SSM model for medical imaging in the literature. With similar aims, few recent studies have proposed SSM-based architectures for medical image reconstruction [45]. However, MambaRoll carries several unique design elements that distinguish it from these SSM-based reconstruction methods. In particular, data-driven SSM models have recently been considered based on single-scale SSM modules for medical image reconstruction in [45], and for MRI reconstruction in [46]. Unlike data-driven models that can suffer from suboptimal performance and generalization, MambaRoll is a physics-driven model that incorporates the imaging operator in an unrolled architecture for improved reconstruction performance. Although [47] proposes a physics-driven SSM model for MRI reconstruction, it uses conventional single-scale SSM blocks similar to the data-driven SSM models in [45], [46]. As such, these previous methods can suffer from limited sensitivity towards contextual

features over relatively large spatial distances. In contrast, MambaRoll leverages an autoregressive SSM model that embodies novel PSSM modules, where PSSM modules process feature maps progressively across multiple spatial scales to enhance fidelity in aggregation of a broad set of contextual features. With these technical advances, we provide the first demonstrations of autoregressive state space modeling for accelerated MRI and sparse-view CT reconstruction tasks in the literature.

III. THEORY

A. Medical Image Reconstruction

In many medical imaging modalities, acquired data and the underlying image that reflects the spatial distribution of tissue structure are associated through a linear system [1]:

$$\mathcal{A}x + \varepsilon = y, \quad (1)$$

where $x \in \mathbb{C}^N$ denotes the underlying complex image in vector form (N : number of pixels), $y \in \mathbb{C}^M$ are acquired complex data in vector form (M : number of measurements), ε is measurement noise, and $\mathcal{A} \in \mathbb{C}^{M \times N}$ is the imaging operator that describes the relationship between image and measurement domains. For MRI scans, $\mathcal{A} = \mathcal{PFC}$ where \mathcal{P} denotes the k-space sampling pattern, \mathcal{F} denotes Fourier transformation, and \mathcal{C} denotes coil sensitivities [22]. Accordingly, \mathcal{A} can be computed based on \mathcal{P} and \mathcal{F} that depend on known scan parameters, and \mathcal{C} that can be estimated from data in a central calibration region. For CT scans, \mathcal{A} can be taken as a Radon transformation \mathcal{R} [2]. Image reconstruction

from acquired measurements then involves solution of the linear system in Eq. 1 by inverting the imaging operator. Such inversion becomes increasingly more ill-conditioned as the number of measurements decline with respect to the number of pixels that are to be resolved [3]. Thus, in challenging tasks such as accelerated MRI and sparse-view CT reconstruction, image priors are employed to improve problem conditioning by regularizing reconstructions:

$$\hat{x} = \arg \min_x \|\mathcal{A}x - y\|_2^2 + R(x), \quad (2)$$

where $R(x)$ denotes an image prior that serves to regularize the reconstructions based on the distribution of high-quality medical images.

In PD models, the solution of Eq. 2 is operationalized as iterations through cascades of an unrolled architecture G_{θ_k} , such that the output of cascade $k \in [1 K]$ depends on the output of the previous cascade [29]:

$$\hat{x}_k = G_{\theta_k}(\hat{x}_{k-1}; \mathcal{A}, y), \quad (3)$$

where θ_k denotes the parameters of the k th cascade, and $\hat{x}_0 = \mathcal{A}^\dagger y$ is a linear reconstruction of undersampled data with \dagger denoting the Hermitian adjoint operator. For a given cascade, $G_{\theta_k}(\hat{x}_{k-1}; \mathcal{A}, y) := \Psi_{dc}(\Psi_{nm}(\hat{x}_{k-1}); \mathcal{A}, y)$ interleaves projection through a network module for regularization, with projection through a data-consistency module for fidelity to acquired data:

$$\Psi_{nm}(v_{in}) = \arg \min_{v_{out}} R_{\theta_k}(v_{out}|v_{in}), \quad (4)$$

$$\Psi_{dc}(v_{in}; \mathcal{A}, y) = v_{in} + \mathcal{A}^\dagger(y - \mathcal{A}v_{in}), \quad (5)$$

where the projection in Eq. 4 can be taken as a forward pass through the network module with input v_{in} and output v_{out} . Reconstruction performance in PD models depends critically on the ability of Ψ_{nm} in separating undersampling artifacts from underlying tissue structure. Previous studies have commonly employed convolutional modules that suffer from limited sensitivity to long-range context, or transformer modules that suffer from an unfavorable trade-off between contextual sensitivity and local precision.

B. MambaRoll

MambaRoll is a novel physics-driven autoregressive state-space model for medical image reconstruction. Unlike previous SSM models for medical image reconstruction [45]–[47], each cascade of MambaRoll embodies a set of physics-driven SSM modules (PSSM) to recover high-resolution medical images gradually across multiple spatial scales, followed by a refinement module that enhances recovery of fine-grained tissue structure. Inspired by the recent success of autoregressive methods in computer vision tasks [56], here we devise PSSM modules to autoregressively predict next-scale feature maps given maps at earlier spatial scales. The proposed PSSM modules serve to enhance image reconstruction by aggregating multi-scale contextual features in medical images, while maintaining consistency to acquired data.

B.1 Network Architecture: Receiving a linear reconstruction of undersampled data as a two-channel input $\hat{x}_0 = \mathcal{A}^\dagger y \in \mathbb{R}^{H \times W \times 2}$ with channels storing real and imaginary

components (H : image height, W : image width), MambaRoll projects its input through K cascades comprising *novel PSSM modules* and refinement modules to compute the reconstruction $\hat{x}_K \in \mathbb{R}^{H \times W \times 2}$. At cascade k , the input image $f_0 = \hat{x}_{k-1} \in \mathbb{R}^{H \times W \times 2}$ is first projected through S consecutive PSSM modules that autoregressively process feature maps across multiple spatial scales:

$$f_s = \text{PSSM}_s(f_{<s}), \quad \text{for } s \in \{1, 2, \dots, S\}, \quad (6)$$

where s denotes the scale index, $f_s \in \mathbb{R}^{H \times W \times 4}$ for $s \geq 1$ (4 channels due to residual data-consistency blocks expressed in Eq. 13), and $f_{<s} := [f_0 f_1 \dots f_{s-1}] \in \mathbb{R}^{H \times W \times (4s-2)}$ is formed by concatenation of feature maps derived by PSSM modules operating at earlier scales. To ensure that PSSM modules are able to process feature maps while maintaining fidelity to acquired data, f_s for all s carry the same spatial dimensionality as the input image \hat{x}_0 . Thus, processing of feature maps at different spatial scales is achieved by adjusting resolution internally within PSSM modules as described below. Following PSSM modules, a refinement module is employed to enhance recovery of structural details based on convolutional layers:

$$\hat{x}_k = \text{Ref}(f_S) := \text{Conv}(\sigma(\text{Conv}(f_S))), \quad (7)$$

where $\hat{x}_k \in \mathbb{R}^{H \times W \times 2}$ is the output of the k th cascade, and σ is a SiLU activation function.

PSSM modules. Diverging from conventional SSM modules, PSSM modules are based on a novel design that enables progressive recovery of images across multiple spatial scales while maintaining fidelity to acquired data at each scale. In particular, a given PSSM_s module at scale s first projects its input $f_{<s} \in \mathbb{R}^{H \times W \times 4s-2}$ through a convolutional encoder to map high-resolution feature maps onto the desired scale:

$$d_s = \text{Enc}_s(f_{<s}) := \sigma(\text{Conv}_{\text{down}}(\sigma(\text{Conv}(f_{<s}))), \quad (8)$$

where $d_s \in \mathbb{R}^{H_s \times W_s \times C_s}$ with $H_s = H/2^{(S-s)}$, $W_s = W/2^{(S-s)}$, $C_s = 2^{(S-s)}C$ (C : number of channels at scale S), and $\text{Conv}_{\text{down}}$ performs spatial downsampling while Conv expands channel dimensionality to C_s .

Afterwards, a shuffled SSM block with residual connection is employed to efficiently capture contextual features at the s th scale as $g_s = \text{SSM}(d_s)$. For this purpose, the downsampled feature map d_s is unshuffled to tile $J \times J$ patches of pixels across the channel dimension [57]. The resultant feature map $\tilde{d}_s \in \mathbb{R}^{H_s/J \times W_s/J \times C_s J^2}$ is transformed onto a sequence $z_s \in \mathbb{R}^{H_s W_s/J^2 \times C_s J^2}$ via a two-dimensional sweep scan, and processed with a discretized state-space model:

$$h_s[n] = \mathbf{A}h_s[n-1] + \mathbf{B}z_s[n], \quad (9)$$

$$\bar{z}_s[n] = \mathbf{C}h_s[n], \quad (10)$$

where $n \in [1 H_s W_s/J^2]$ denotes sequence index, h_s denotes the scale-specific hidden state, and $\mathbf{A} \in \mathbb{R}^{D,D}$, $\mathbf{B} \in \mathbb{R}^{D,1}$, $\mathbf{C} \in \mathbb{R}^{1,D}$ are learnable parameters (D : the state dimensionality). In Eqs. 9-10, \mathbf{B} and \mathbf{C} are defined as functions of z_s as in selective SSM variants to enable input-dependent filtering [58]. The output sequence \bar{z}_s is expanded and pixel-shuffled [57] to restore the feature map $\bar{d}_s \in \mathbb{R}^{H_s \times W_s \times C_s}$, which is residually added onto the input:

$$g_s = \bar{d}_s + d_s. \quad (11)$$

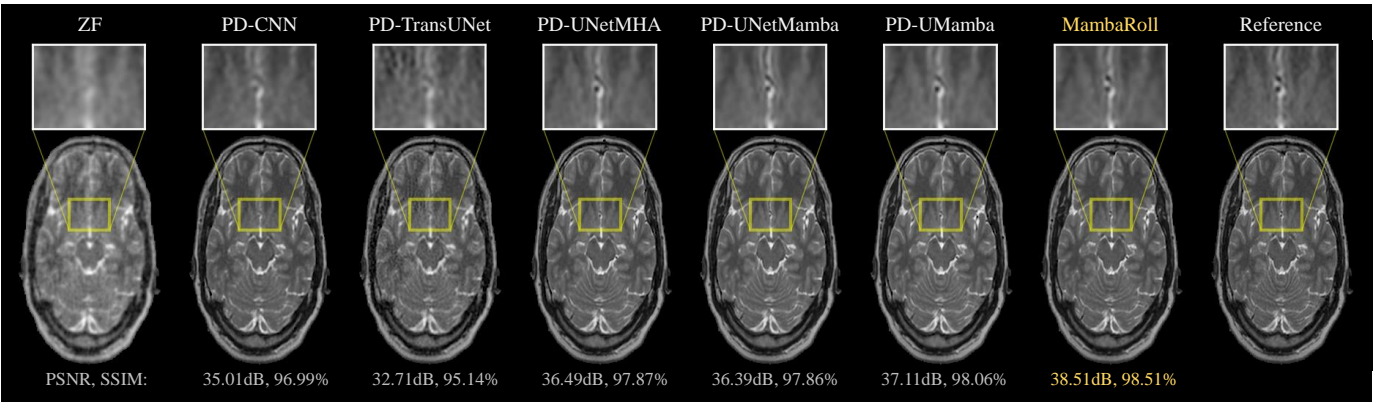


Fig. 2: Accelerated MRI reconstructions of a representative cross-section from a T_2 -weighted acquisition in IXI at $R = 8$. Reconstructed images from competing methods are shown along with a linear reconstruction of undersampled data (ZF), and the reference image derived from fully-sampled data. Zoom-in windows are included to highlight regions where methods show differences in tissue depiction.

TABLE I: Accelerated MRI reconstruction performance on IXI at $R = 4, 8$. Results averaged across different contrasts. PSNR (dB) and SSIM (%) listed as mean \pm std across the test set. Boldface marks the top performing method.

	$R = 4$		$R = 8$	
	PSNR	SSIM	PSNR	SSIM
MambaRoll	48.16\pm2.25	99.72\pm0.08	40.56\pm1.38	98.87\pm0.21
PD-UMamba	46.09 \pm 1.87	99.60 \pm 0.09	39.24 \pm 1.16	98.58 \pm 0.23
PD-UNetMamba	45.65 \pm 1.80	99.56 \pm 0.10	38.74 \pm 1.12	98.45 \pm 0.25
PD-UNetMHA	45.67 \pm 1.84	99.56 \pm 0.10	38.76 \pm 1.10	98.46 \pm 0.25
PD-TransUNet	39.27 \pm 1.11	98.48 \pm 0.33	34.71 \pm 1.16	96.37 \pm 0.86
PD-CNN	42.22 \pm 1.64	99.11 \pm 0.18	36.65 \pm 1.05	97.68 \pm 0.36

To enable PSSM modules to enforce fidelity to acquired data, the contextualized feature map g_s is projected through a convolutional decoder to recollect a high-resolution image:

$$u_s = \text{Dec}_s(g_s) := \text{Conv}(\sigma(\text{Conv}_{\text{up}}(g_s))), \quad (12)$$

where $u_s \in \mathbb{R}^{H \times W \times 2}$, Conv_{up} performs spatial upsampling while Conv reduces channel dimensionality to 2 to store real and imaginary components. Finally, the recollected image can be projected through a residual data-consistency block that concatenates u_s with a data-consistent version of itself:

$$f_s = \text{resDC}(u_s) := [u_s \quad (u_s + \mathcal{A}^\dagger(y - \mathcal{A}u_s))], \quad (13)$$

where the second term ensures that reconstructed data are consistent with acquired data y for the subset of collected spatial encodings in measurement domain. This design allows the model to have fine-grained control over the emphasis on data consistency to optimize task performance.

B.2 Autoregressive Learning Objective: MambaRoll leverages autoregressive processing across multiple spatial scales via PSSM modules, which compute contextualized feature maps g_s at each scale that are decoded to high-resolution images u_s in order to promote fidelity of acquired data. In principle, u_s can be expected to match the ground-truth images closely in a performant reconstruction model. Thus, we propose to train MambaRoll via the following objective:

$$\mathcal{L}_{\text{MambaRoll}} = \|\hat{x}_K - x_K\|_2^2 + \lambda \sum_{s=1}^S \|\text{Dec}_s(g_s)_K - x_K\|_2^2, \quad (14)$$

where the first loss term is defined between the model output and the reference image, the second term is defined between scale-specific decoded images (at the K th cascade) and the

reference image, and λ is a regularization weight.

IV. METHODS

A. Datasets

A.1 Accelerated MRI: Experiments were conducted on brain MRI data from IXI¹ and fastMRI [59] datasets. For each subject in IXI, three volumes with T_1 , T_2 and PD contrasts were analyzed as single-coil acquisitions, where each volume comprised 100 cross-sections with brain tissue. Data were split into non-overlapping training, validation, test sets composed of (21, 15, 30) subjects. For each subject in fastMRI, three volumes with T_1 , T_2 and FLAIR contrasts were analyzed as multi-coil complex k-space data, where each volume comprised 10 cross-sections. Multi-coil data were coil compressed onto 5 virtual coils while preserving 90% of data variance [60], and coil sensitivities were estimated via ESPIRiT [61]. Data were split into training, validation, test sets of (240, 60, 120) subjects. Accelerated MRI scans were obtained via two-dimensional variable-density undersampling at rates $R = 4 - 8$ [62]. Linear reconstructions of undersampled data were obtained by zero-filling missing k-space samples, followed by inverse Fourier transformations. Each cross-section was reconstructed separately.

A.2 Sparse-view CT: Experiments were conducted on lung CT data from the LoDoPaB-CT dataset [63]. For each subject, a single volume was analyzed comprising 90 cross-sections of size 352×352 . Data were split into non-overlapping training, validation, test sets composed of (30, 6, 12) subjects. To obtain sparse-view CT scans, ground-truth reconstructions in LoDoPaB-CT were Radon transformed based on a two-dimensional parallel-beam geometry, and sinograms were undersampled at rates $R = 4 - 6$ across the angular dimension. Linear reconstructions of undersampled data were obtained via filtered back projection (FBP). Each cross-section was reconstructed separately.

B. Architectural Details

In each cascade of its unrolled architecture, MambaRoll used PSSM modules for autoregressive prediction across $S =$

¹<https://brain-development.org/ixi-dataset/>

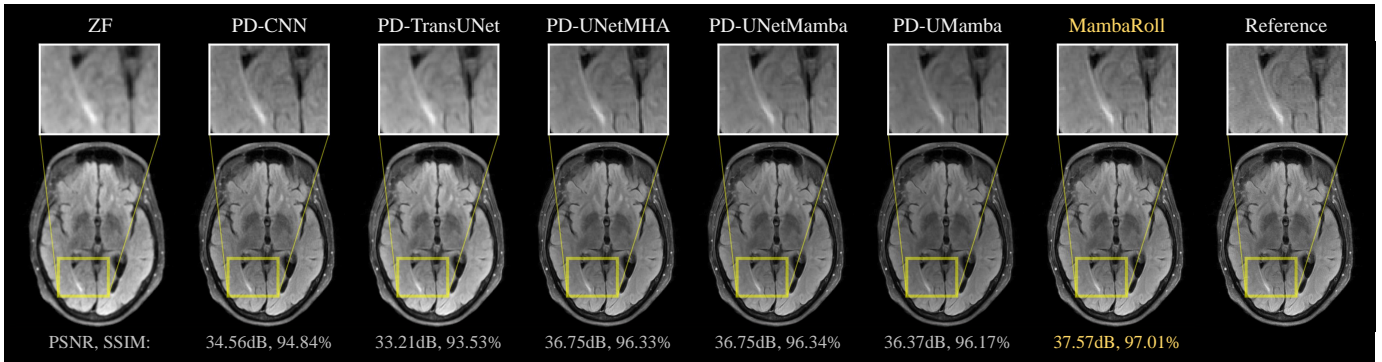


Fig. 3: Accelerated MRI reconstructions of a representative cross-section from a FLAIR-weighted acquisition in fastMRI at $R = 8$. Reconstructed images from competing methods are shown along with a linear reconstruction of undersampled data (ZF), and the reference image derived from fully-sampled data. Zoom-in windows are included to highlight regions where methods show differences in tissue depiction.

TABLE II: Accelerated MRI reconstruction performance on fastMRI at $R = 4, 8$. Results averaged across different contrasts. PSNR (dB) and SSIM (%) listed as mean \pm std across the test set. Boldface marks the top performing method.

	$R = 4$		$R = 8$	
	PSNR	SSIM	PSNR	SSIM
MambaRoll	45.28\pm3.48	98.59\pm2.71	39.59\pm2.88	96.13\pm3.76
PD-UMamba	42.79 \pm 3.16	97.75 \pm 2.55	38.45 \pm 2.81	94.90 \pm 4.09
PD-UNetMamba	43.34 \pm 3.50	97.79 \pm 3.79	38.84 \pm 3.37	95.03 \pm 4.96
PD-UNetMHA	43.41 \pm 3.30	97.96 \pm 2.18	38.91 \pm 3.03	95.24 \pm 3.95
PD-TransUNet	38.49 \pm 3.05	95.97 \pm 3.34	35.80 \pm 2.68	93.39 \pm 4.84
PD-CNN	41.21 \pm 2.49	97.42 \pm 2.20	37.06 \pm 2.42	94.85 \pm 3.75

3 spatial scales (at 0.25, 0.5, 1 scale of the original image resolution), and a refinement module to provide the cascade output. Each PSSM module received feature maps from the previous cascade as input, along with features maps at earlier scales in the current cascade. The PSSM module comprised a convolutional encoder to downsample feature maps to the target scale, a shuffled SSM block to model spatial context, a convolutional decoder to upsample feature maps, and a residual data-consistency block. The encoder used expansion factors across the channel dimension of (4, 2, 1), whereas the decoder used expansion factors of (0.25, 0.5, 1) across scales. The SSM block used a pixel-shuffle factor of $J = 4$ and a sweep-scan trajectory to project feature maps onto a sequence, and a state-dimensionality of $D = 64$. The refinement module comprised a convolutional block. All convolution layers used a 3×3 kernel size and SiLU activation functions.

C. Competing Methods

MambaRoll was demonstrated against physics-driven models that used state-of-the-art network modules based on convolutional (PD-CNN), transformer (PD-TransUNet, PD-UNetMHA), or SSM backbones (PD-UNetMamba, PD-UMamba). For each method, key hyperparameters including the number of cascades in the unrolled architecture (K) and learning rate were selected to maximize performance on the validation set. Network models used two separate input-output channels to represent real and imaginary components of MR images, and a single input-output channel for CT images. Modeling was performed via the PyTorch framework on an Nvidia RTX 4090 GPU. Models were trained via the Adam

optimizer for 50 epochs, $(\beta_1, \beta_2) = (0.9, 0.999)$, and cosine annealing of learning rates in the range $[\eta_{min}, \eta_{max}]$.

PD-CNN: A convolutional module based on convolutional layers processing feature maps at the original image resolution was considered [29]. $K=5$, $\eta_{min}=10^{-7}$, $\eta_{max}=5 \times 10^{-6}$ in IXI; $K=5$, $\eta_{min}=10^{-5}$, $\eta_{max}=2 \times 10^{-4}$ in fastMRI; $K=5$, $\eta_{min}=10^{-7}$, $\eta_{max}=5 \times 10^{-6}$ in LoDoPaB-CT were used.

PD-TransUNet: A transformer module based on a UNet backbone equipped with a ViT block in the bottleneck was considered [49]. $K=5$, $\eta_{min}=10^{-5}$, $\eta_{max}=10^{-3}$ were used.

PD-UNetMHA: A transformer module based on a UNet backbone equipped with self-attention layers was considered [64]. $K=5$, $\eta_{min}=10^{-5}$, $\eta_{max}=2 \times 10^{-4}$ were used.

PD-UNetMamba: An SSM module interleaving convolutional and Mamba blocks in a UNet-style backbone was considered [65]. $K=5$, $\eta_{min}=10^{-5}$, $\eta_{max}=2 \times 10^{-4}$ were used.

PD-UMamba: An SSM module based on a UNet-style backbone equipped with Mamba blocks was considered [43]. $K=5$, $\eta_{min}=10^{-5}$, $\eta_{max}=2 \times 10^{-4}$ were used.

MambaRoll: The proposed model was implemented with $K=5$, $\eta_{min}=10^{-5}$, $\eta_{max}=2 \times 10^{-4}$.

D. Analyses

Models were trained and tested on two-dimensional cross sections. Reconstruction performance was assessed by quantifying peak signal-to-noise ratio (PSNR) and structural similarity index (SSIM) between recovered and reference images. Reference images were derived via Fourier reconstruction of fully-sampled acquisitions for MRI scans, and via filtered back-projection of fully-sampled sinograms in CT scans. Significance of performance differences among competing methods were assessed via Wilcoxon signed-rank tests.

V. RESULTS

A. Accelerated MRI Reconstruction

Demonstrations were first performed for accelerated MRI reconstruction. MambaRoll was compared against PD models equipped with state-of-the-art network modules including convolutional (PD-CNN), transformer (PD-TransUNet, PD-UNetMHA), and SSM (PD-UNetMamba, PD-UMamba) back-

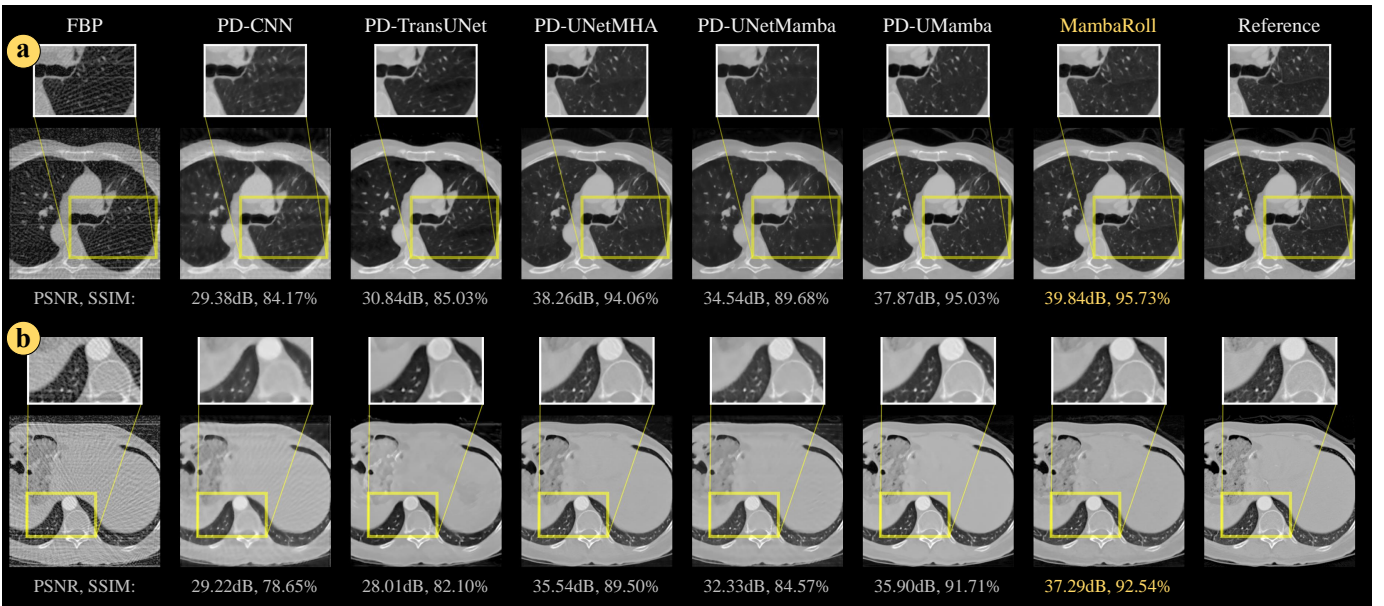


Fig. 4: Sparse-view CT reconstructions of two representative cross-sections (a),(b) in LoDoPaB-CT at $R = 6$. Reconstructed images from competing methods are shown along with a linear reconstruction of undersampled data (FBP), and the reference image derived from fully-sampled data. Zoom-in windows are included to highlight regions where methods show differences in tissue depiction.

bones. Performance metrics for reconstructions of undersampled data at rates $R = 4, 8$ are listed in Table I for IXI and Table II for fastMRI datasets. We find that MambaRoll significantly outperforms all competing methods, consistently across reconstruction tasks ($p < 0.05$). On average across tasks, Mamba offers (PSNR, SSIM) improvements of 4.1dB, 1.1% over convolutional; 4.0dB, 1.4% over transformer; and 1.8dB, 0.6% over SSM baselines.

Representative reconstructions from competing methods are depicted in Fig. 2 for IXI and in Fig. 3 for fastMRI. In general, PD-CNN suffers from notable spatial blur and residual noise; PD-TransUNet can suffer from spatial blur and pixel-intensity artifacts; PD-UNetMHA, PD-UNetMamba and PD-UMamba show inaccuracies in contrast depiction due to suboptimal spatial acuity that cause fading of some fine-grained tissue structures. In comparison, MambaRoll produces more accurate depiction of tissue structure and contrast, along with relatively lower artifacts and noise than baselines.

B. Sparse-view CT Reconstruction

Next, demonstrations were performed for sparse-view CT reconstruction. MambaRoll was compared against PD models equipped with state-of-the-art network modules including convolutional (PD-CNN), transformer (PD-TransUNet, PD-UNetMHA), and SSM (PD-UNetMamba, PD-UMamba) backbones. Performance metrics for reconstructions of undersampled data at rates $R = 4, 6$ are listed in Table III for the LoDoPaB-CT dataset. We find that MambaRoll significantly outperforms all competing methods, consistently across reconstruction tasks ($p < 0.05$). On average across tasks, Mamba offers (PSNR, SSIM) improvements of 8.7dB, 11.4% over convolutional; 5.6dB, 6.2% over transformer; and 2.2dB, 2.5% over SSM baselines.

Representative images from sparse-view CT reconstructions

TABLE III: Sparse-view CT reconstruction performance on LoDoPaB-CT at $R = 4, 6$. PSNR (dB) and SSIM (%) listed as mean \pm std across the test set. Boldface marks the top-performing method.

	$R = 4$		$R = 6$	
	PSNR	SSIM	PSNR	SSIM
MambaRoll	40.49\pm3.50	93.82\pm4.89	38.47\pm3.06	91.62\pm5.90
PD-UMamba	40.12 \pm 3.16	93.76 \pm 4.88	37.18 \pm 2.54	90.76 \pm 5.96
PD-UNetMamba	37.31 \pm 2.43	90.83 \pm 5.66	34.33 \pm 1.91	85.62 \pm 6.43
PD-UNetMHA	37.16 \pm 2.38	90.49 \pm 5.56	37.10 \pm 2.55	89.99 \pm 6.28
PD-TransUNet	31.73 \pm 1.30	85.14 \pm 6.65	29.72 \pm 1.03	80.38 \pm 7.00
PD-CNN	31.38 \pm 1.00	81.91 \pm 5.59	30.14 \pm 1.05	80.66 \pm 6.29

are depicted in Fig. 4. Among baselines, PD-CNN and PD-TransUNet show notable reconstruction errors due to spatial blurring and residual streaking artifacts; whereas PD-UNetMHA, PD-UNetMamba and PD-UMamba suffer from moderate streaking artifacts that occasionally manifest as contrast inaccuracies near regions of bright tissue signals. In comparison, MambaRoll produces more accurate depiction of tissue structure and contrast, and relatively lower artifacts and noise than baselines.

C. Ablation Studies

We conducted ablation studies to evaluate the influence of major architectural elements of MambaRoll to reconstruction performance. To assess the importance of novel PSSM modules, we trained a ‘w/o PSSM’ variant that removed the PSSM modules albeit retained the refinement modules so as to create an unrolled architecture based on a convolutional network module. To assess the importance of autoregressive modeling across spatial scales, we trained a ‘w/o AR’ variant that used a PSSM module operating at a single spatial scale where feature maps retained the resolution of original input images. To assess the importance of data-consistency blocks, we trained a ‘w/o DC’ variant that ablated DC blocks albeit

TABLE IV: Performance of MambaRoll variants on representative reconstruction tasks. A ‘w/o PSSM’ variant ablating PSSM modules, a ‘w/o AR’ variant ablating autoregressive processing, a ‘w/o DC’ variant ablating data-consistency modules, and a ‘w MHSA’ variant that replaced SSM blocks with multi-head self-attention layers were considered.

	IXI - T ₁ , R = 4		fastMRI - FLAIR, R = 4		CT, R = 4	
	PSNR	SSIM	PSNR	SSIM	PSNR	SSIM
MambaRoll	45.53±1.04	99.65±0.07	43.65±3.31	98.36±1.49	40.49±3.50	93.82±4.89
w/o PSSM	42.35±0.94	99.35±0.13	40.51±2.98	96.91±2.27	36.55±2.31	90.10±5.46
w/o AR	43.24±1.08	99.46±0.12	37.34±2.70	94.31±3.75	37.16±2.44	90.79±4.96
w/o DC	34.59±0.46	96.94±0.33	36.37±2.50	92.21±3.45	37.61±2.62	91.29±5.23
w MHSA	43.34±1.22	99.47±0.13	40.95±3.04	97.13±2.25	38.45±2.87	91.95±5.09

retaining their residual connections to create a purely data-driven SSM model. Lastly, to assess the importance of SSM layers in capturing contextual features in medical images, we trained a ‘w MHSA’ variant that replaced SSM layers with a multi-head self-attention layer as in transformer modules. Table IV lists performance metrics for all MambaRoll variants. We find that MambaRoll yields superior performance against all variants, corroborating the importance of all architectural design elements in performing high-fidelity medical image reconstruction.

VI. DISCUSSION

The performance and utility of the proposed method might benefit from several technical improvements. A first group of improvements concern the learning setup for medical image reconstruction. Here, demonstrations were performed in a supervised setup where the training set comprises fully-sampled acquisitions as ground truth. To enable training on datasets comprising solely undersampled data, self-supervised learning approaches could be adopted [66]–[68]. In cases where the training set mixes a first subject pool with fully-sampled data and a second subject pool with undersampled data, a hybrid learning strategy might be adopted where self-supervised training on undersampled data could be followed by supervised fine-tuning [30]. Alternatively, cycle-consistent learning could be adopted to enhance training efficacy on such unpaired datasets [69].

A second group of improvements concern the loss functions used to express the learning objective. Here, we observed high-quality reconstruction of both MRI and CT images based on models trained via autoregressive image prediction across multiple spatial scales. Recent studies suggest that such autoregressive modeling might be a powerful alternative to other generative approaches based on adversarial and diffusive losses [56]. Yet, autoregressive predictions based on pixel-wise loss terms can be combined with generative losses to seek further realism and sensitivity to fine details in medical images [70], [71]. While our primary focus in the current study was on architectural design of reconstruction models, MambaRoll can be combined with generative learning objectives to examine their potential benefits in future work [72], [73]. In applications where it is difficult to curate a training set altogether, test-time adaptation procedures could instead be employed for subject-specific tuning of model weights at the expense of elevated inference burden, and the learning objective can be expressed based on consistency to acquired data in such cases

[18], [74], [75].

A third group of improvements concern the reconstruction tasks examined. Here, we built models that process single-modality images (i.e., single MRI contrast, single CT contrast). Recent work suggests that state space models can also be helpful in joint reconstructions of multi-modality images [46]. A basic approach to extent MambaRoll for multi-modal reconstruction would be to assign separate channels per modality in the input-output layers and across data-consistency layers in PSSM modules [15], [76]. Separate model branches could also be employed to process each modality [77], while cross-modality interactions are mediated by attentional or state-space modules for fine-grained control of feature representations shared between modalities [46], [78].

A fourth group of improvements concern the architectural design of MambaRoll. Here, scale-specific convolutional layers were used in PSSM modules to downsample/upsample feature maps in order to permit autoregressive state-space modeling across spatial scales. This design outperformed variant models that used transformers to capture contextual representations, including a hybrid architecture that intermittently injected Mamba blocks within CNN backbones (e.g., UNetMamba) [28], and a purely Mamba-based architecture (e.g., UMamba) [79]. These findings suggest that MambaRoll maintains an improved balance between local and global sensitivity against these alternative approaches. Yet, improvements in contextual sensitivity might be possible by combining attentional and SSM-based features, or by combining autoregressive modeling across scales with autoregression across spatial dimensions [80]. Future work is warranted to explore potential benefits of hybrid designs.

Lastly, here we considered single-domain models that primarily process features maps in image domain. Previous studies on medical image reconstruction have reported that dual-domain architectures can offer additional benefits by employing separate branches to process data in measurement and image domains. While we did not examine the influence of processing domains on reconstruction performance in the current study, we reason that a multi-domain version of MambaRoll would enjoy similar benefits to multi-domain models based on other architectures such as CNNs or transformers [36], [41].

VII. CONCLUSION

In this study, we introduced a novel deep learning method for medical image reconstruction, MambaRoll, based on

physics-driven autoregressive state space modeling. MambaRoll leverages autoregressive prediction across multiple spatial scales along with physics-driven SSM modules to effectively aggregate contextual features in medical images. Demonstrations on accelerated MRI and sparse-view CT reconstructions indicate that the proposed model consistently outperforms state-of-the-art methods in terms of image quality, without compromising computational efficiency. Therefore, MambaRoll holds great potential for improving utility of learning-based medical image reconstruction.

REFERENCES

- [1] J. C. Ye, Y. C. Eldar, and M. Unser, *Deep Learning for Biomedical Image Reconstruction*. Cambridge: Cambridge University Press, 2023.
- [2] G. Wang, J. C. Ye, K. Mueller, and J. A. Fessler, "Image reconstruction is a new frontier of machine learning," *IEEE Trans. Med. Imaging*, vol. 37, no. 6, p. 1289–1296, 2018.
- [3] G. Wang, J. C. Ye, and B. D. Man, "Deep learning for tomographic image reconstruction," *Nature Mach. Intell.*, vol. 2, no. 12, p. 737–748, 2020.
- [4] S. K. Zhou, H. Greenspan, C. Davatzikos, J. S. Duncan, B. Van Ginneken, A. Madabhushi, J. L. Prince, D. Rueckert, and R. M. Summers, "A Review of Deep Learning in Medical Imaging: Imaging Traits, Technology Trends, Case Studies With Progress Highlights, and Future Promises," *Proc. IEEE*, vol. 109, no. 5, pp. 820–838, 2021.
- [5] J. Schlemper, J. Caballero, J. V. Hajnal, A. Price, and D. Rueckert, "A Deep Cascade of Convolutional Neural Networks for MR Image Reconstruction," in *IPMI*, 2017, pp. 647–658.
- [6] S. Wang, Z. Su, L. Ying, X. Peng, S. Zhu, F. Liang, D. Feng, and D. Liang, "Accelerating magnetic resonance imaging via deep learning," in *IEEE ISBI*, 2016, pp. 514–517.
- [7] D. Lee, J. Yoo, S. Tak, and J. C. Ye, "Deep residual learning for accelerated mri using magnitude and phase networks," *IEEE Trans. Biomed. Eng.*, vol. 65, no. 9, pp. 1985–1995, 2018.
- [8] Y. Han and J. C. Ye, "Framing u-net via deep convolutional framelets: Application to sparse-view ct," *arXiv:1708.08333*, 2018.
- [9] H. Chen, Y. Zhang, M. K. Kalra, F. Lin, Y. Chen, P. Liao, J. Zhou, and G. Wang, "Low-dose ct with a residual encoder-decoder convolutional neural network," *IEEE Trans. Med. Imaging*, vol. 36, no. 12, pp. 2524–2535, 2017.
- [10] W. Wu, D. Hu, C. Niu, H. Yu, V. Vardhanabhuti, and G. Wang, "DRONE: Dual-Domain Residual-based Optimization Network for Sparse-View CT Reconstruction," *IEEE Trans. Med. Imaging*, vol. 40, no. 11, pp. 3002–3014, 2021.
- [11] M. Lee, H. Kim, and H.-J. Kim, "Sparse-view ct reconstruction based on multi-level wavelet convolution neural network," *Phys. Med.*, vol. 80, pp. 352–362, 2020.
- [12] Z. Zhang, X. Liang, X. Dong, Y. Xie, and G. Cao, "A sparse-view ct reconstruction method based on combination of densenet and deconvolution," *IEEE Trans. Med. Imaging*, vol. 37, no. 6, pp. 1407–1417, 2018.
- [13] G. Yang, S. Yu, H. Dong, G. Slabaugh, P. L. Dragotti, X. Ye, F. Liu, S. Arridge, J. Keegan, Y. Guo *et al.*, "DAGAN: Deep de-aliasing generative adversarial networks for fast compressed sensing MRI reconstruction," *IEEE Trans. Med. Imaging*, vol. 37, no. 6, pp. 1310–1321, 2018.
- [14] M. Mardani, E. Gong, J. Y. Cheng, S. Vasanawala, G. Zaharchuk, L. Xing, and J. M. Pauly, "Deep generative adversarial neural networks for compressive sensing MRI," *IEEE Trans. Med. Imaging*, vol. 38, no. 1, pp. 167–179, 2019.
- [15] S. U. Dar, M. Yurt, M. Shahdloo, M. E. Ildiz, B. Tınaz, and T. Çukur, "Prior-guided image reconstruction for accelerated multi-contrast mri via generative adversarial networks," *IEEE J. Sel. Top. Signal Process.*, vol. 14, no. 6, pp. 1072–1087, 2020.
- [16] A. Jalal, M. Arvinte, G. Daras, E. Price, A. G. Dimakis, and J. Tamir, "Robust compressed sensing mri with deep generative priors," in *Adv. Neural Inf. Process. Sys.*, vol. 34, 2021, pp. 14938–14954.
- [17] W. Xia, W. Cong, and G. Wang, "Patch-based denoising diffusion probabilistic model for sparse-view ct reconstruction," *arXiv:2211.10388*, 2022.
- [18] A. Güngör, S. U. Dar, Ş. Öztürk, Y. Korkmaz, G. Elmas, M. Özbey, and T. Çukur, "Adaptive diffusion priors for accelerated MRI reconstruction," *Med. Image Anal.*, vol. 88, p. 102872, 2023.
- [19] K. H. Jin, M. T. McCann, E. Froustey, and M. Unser, "Deep convolutional neural network for inverse problems in imaging," *IEEE Trans. Image Process.*, vol. 26, no. 9, pp. 4509–4522, 2017.
- [20] U. S. Kamilov, C. A. Bouman, G. T. Buzzard, and B. Wohlberg, "Plug-and-play methods for integrating physical and learned models in computational imaging: Theory, algorithms, and applications," *IEEE Signal Process. Mag.*, vol. 40, no. 1, pp. 85–97, 2023.
- [21] G. Elmas, S. U. Dar, Y. Korkmaz, E. Ceyani, B. Susam, M. Özbey, S. Avestimehr, and T. Çukur, "Federated learning of generative image priors for mri reconstruction," *IEEE Trans. Med. Imaging*, vol. 42, no. 7, pp. 1996–2009, 2023.
- [22] K. Hammernik, T. Küstner, B. Yaman, Z. Huang, D. Rueckert, F. Knoll, and M. Akçakaya, "Physics-driven deep learning for computational magnetic resonance imaging," *arXiv:2203.12215*, 2022.
- [23] K. Hammernik, T. Klatzer, E. Kobler, M. P. Recht, D. K. Sodickson, T. Pock, and F. Knoll, "Learning a variational network for reconstruction of accelerated MRI data," *Magn. Reson. Med.*, vol. 79, no. 6, pp. 3055–3071, 2017.
- [24] Y. Zhang, D. Hu, S. Hao, J. Liu, G. Quan, Y. Zhang, X. Ji, and Y. Chen, "Dream-net: Deep residual error iterative minimization network for sparse-view ct reconstruction," *IEEE J. Biomed. Health Inf.*, vol. 27, no. 1, pp. 480–491, 2023.
- [25] H. Zhang, B. Liu, H. Yu, and B. Dong, "MetaInv-Net: Meta Inversion Network for Sparse View CT Image Reconstruction," *IEEE Trans. Med. Imaging*, vol. 40, no. 2, pp. 621–634, 2021.
- [26] B. Zhou and S. K. Zhou, "DuDoRNet: Learning a Dual-Domain Recurrent Network for Fast MRI Reconstruction With Deep T1 Prior," in *IEEE/CVF Comput. Vis. Pattern. Recognit.*, 2020.
- [27] S. A. H. Hosseini, B. Yaman, S. Moeller, M. Hong, and M. Akçakaya, "Dense recurrent neural networks for accelerated mri: History-cognizant unrolling of optimization algorithms," *IEEE J. Select. Top. Signal Process.*, vol. 14, no. 6, pp. 1280–1291, 2020.
- [28] O. Dalmaz, M. Yurt, and T. Çukur, "ResViT: Residual vision transformers for multi-modal medical image synthesis," *IEEE Trans. Med. Imaging*, vol. 41, no. 10, pp. 2598–2614, 2022.
- [29] H. K. Aggarwal, M. P. Mani, and M. Jacob, "MoDL: Model-Based deep learning architecture for inverse problems," *IEEE Trans. Med. Imaging*, vol. 38, no. 2, pp. 394–405, 2019.
- [30] S. U. H. Dar, M. Özbey, A. B. Çatlı, and T. Çukur, "A transfer-learning approach for accelerated mri using deep neural networks," *Magn. Reson. Med.*, vol. 84, no. 2, pp. 663–685, 2020.
- [31] J. Xiang, Y. Dong, and Y. Yang, "FISTA-Net: Learning a Fast Iterative Shrinkage Thresholding Network for Inverse Problems in Imaging," *IEEE Trans. Med. Imaging*, vol. 40, no. 5, pp. 1329–1339, 2021.
- [32] C. Wang, K. Shang, H. Zhang, Q. Li, Y. Hui, and S. K. Zhou, "DuDo-Trans: Dual-Domain Transformer Provides More Attention for Sinogram Restoration in Sparse-View CT Reconstruction," *arXiv:2111.10790*, 2021.
- [33] W. Xia, Z. Yang, Z. Lu, Z. Wang, and Y. Zhang, "Regformer: A local-nonlocal regularization-based model for sparse-view ct reconstruction," *IEEE Trans. Rad. Plasma Med. Sci.*, vol. 8, no. 2, pp. 184–194, 2024.
- [34] Y. Korkmaz, S. U. Dar, M. Yurt, M. Özbey, and T. Çukur, "Unsupervised mri reconstruction via zero-shot learned adversarial transformers," *IEEE Trans. Med. Imaging*, vol. 41, no. 7, pp. 1747–1763, 2022.
- [35] J. Huang, Y. Fang, Y. Wu, H. Wu, Z. Gao, Y. Li, J. Del Ser, J. Xia, and G. Yang, "Swin transformer for fast MRI," *Neurocomputing*, vol. 493, pp. 281–304, 2022.
- [36] P. Guo, Y. Mei, J. Zhou, S. Jiang, and V. M. Patel, "Reconformer: Accelerated mri reconstruction using recurrent transformer," *arXiv:2201.09376*, 2022.
- [37] K. Lin and R. Heckel, "Vision transformers enable fast and robust accelerated MRI," in *Med. Imaging Deep Learn.*, vol. 172, 2022, pp. 774–795.
- [38] B. Zhou, N. Dey, J. Schlemper, S. S. M. Salehi, C. Liu, J. S. Duncan, and M. Sofka, "DSFormer: A Dual-domain Self-supervised Transformer for Accelerated Multi-contrast MRI Reconstruction," *arXiv:2201.10776*, 2022.
- [39] Y. Korkmaz, T. Çukur, and V. M. Patel, "Self-supervised mri reconstruction with unrolled diffusion models," in *Med. Image Comput. Comput. Assist. Int.* Springer, 2023, pp. 491–501.
- [40] Z. Zhang, L. Yu, X. Liang, W. Zhao, and L. Xing, "Transct: dual-path transformer for low dose computed tomography," in *Med. Image Comput. Assist. Int.* Springer, 2021, pp. 55–64.
- [41] C.-M. Feng, Y. Yan, G. Chen, Y. Xu, Y. Hu, L. Shao, and H. Fu, "Multimodal transformer for accelerated mr imaging," *IEEE Trans. Med. Imaging*, vol. 42, no. 10, pp. 2804–2816, 2023.

- [42] L. Zhu, B. Liao, Q. Zhang, X. Wang, W. Liu, and X. Wang, "Vision mamba: Efficient visual representation learning with bidirectional state space model," *arXiv:2401.09417*, 2024.
- [43] J. Ma, F. Li, and B. Wang, "U-Mamba: Enhancing Long-range Dependency for Biomedical Image Segmentation," *arXiv:2401.04722*, 2024.
- [44] J. Liu, H. Yang, H.-Y. Zhou, Y. Xi, L. Yu, C. Li, Y. Liang, G. Shi, Y. Yu, S. Zhang *et al.*, "Swin-umamba: Mamba-based unet with imagenet-based pretraining," in *Med. Image Comput. Comput. Assist. Int.* Springer, 2024, pp. 615–625.
- [45] J. Huang, L. Yang, F. Wang, Y. Wu, Y. Nan, W. Wu, C. Wang, K. Shi, A. I. Aviles-Rivero, C.-B. Schönlieb *et al.*, "Enhancing global sensitivity and uncertainty quantification in medical image reconstruction with monte carlo arbitrary-masked mamba," *Med. Image Anal.*, vol. 99, p. 103334, 2025.
- [46] J. Zou, L. Liu, Q. Chen, S. Wang, Z. Hu, X. Xing, and J. Qin, "MMR-Mamba: Multi-Modal MRI Reconstruction with Mamba and Spatial-Frequency Information Fusion," *arXiv:2406.18950*, 2024.
- [47] Y. Korkmaz and V. M. Patel, "MambaRecon: MRI Reconstruction with Structured State Space Models," *arXiv:2409.12401*, 2024.
- [48] O. F. Atli, B. Kabas, F. Arslan, M. Yurt, O. Dalmaz, and T. Çukur, "I2I-Mamba: Multi-modal medical image synthesis via selective state space modeling," *arXiv:2405.14022*, 2024.
- [49] J. Chen, Y. Lu, Q. Yu, X. Luo, E. Adeli, Y. Wang, L. Lu, A. L. Yuille, and Y. Zhou, "TransUNet: Transformers make strong encoders for medical image segmentation," *arXiv:2102.04306*, 2021.
- [50] D. Wu, K. Kim, G. E. Fakhri, and Q. Li, "A cascaded convolutional neural network for x-ray low-dose ct image denoising," *arXiv:1705.04267*, 2017.
- [51] J. Yuan, F. Zhou, Z. Guo, X. Li, and H. Yu, "Hcformer: hybrid cnn-transformer for ldct image denoising," *J. Dig. Imaging*, vol. 36, no. 5, pp. 2290–2305, 2023.
- [52] A. Güngör, B. Askin, D. A. Soydan, E. U. Saritas, C. B. Top, and T. Çukur, "TranSMS: Transformers for Super-Resolution Calibration in Magnetic Particle Imaging," *IEEE Trans. Med. Imaging*, vol. 41, no. 12, pp. 3562–3574, 2022.
- [53] M. Heidari, S. G. Kolahi, S. Karimijafarbigloo, B. Azad, A. Bozorgpour, S. Hatami, R. Azad, A. Diba, U. Bagci, D. Merhof *et al.*, "Computation-efficient era: A comprehensive survey of state space models in medical image analysis," *arXiv:2406.03430*, 2024.
- [54] H. A. Bedel, I. Sivgin, O. Dalmaz, S. U. Dar, and T. Çukur, "BoIT: Fused window transformers for fMRI time series analysis," *Med. Image Anal.*, vol. 88, p. 102841, 2023.
- [55] Z. Xing, T. Ye, Y. Yang, G. Liu, and L. Zhu, "Segmamba: Long-range sequential modeling mamba for 3d medical image segmentation," in *Med. Image Comput. Comput. Assist. Int.* Springer, 2024, pp. 578–588.
- [56] K. Tian, Y. Jiang, Z. Yuan, B. Peng, and L. Wang, "Visual Autoregressive Modeling: Scalable Image Generation via Next-Scale Prediction," *arXiv:2404.02905*, 2024.
- [57] W. Shi, J. Caballero, F. Huszár, J. Totz, A. P. Aitken, R. Bishop, D. Rueckert, and Z. Wang, "Real-time single image and video super-resolution using an efficient sub-pixel convolutional neural network," *arXiv:1609.05158*, 2016.
- [58] Y. Liu, Y. Tian, Y. Zhao, H. Yu, L. Xie, Y. Wang, Q. Ye, and Y. Liu, "Vmamba: Visual state space model," 2024.
- [59] F. Knoll, J. Zbontar, A. Sriram, M. J. Muckley, M. Bruno, A. Defazio, M. Parente, K. J. Geras, J. Katsnelson, H. Chandarana *et al.*, "fastMRI: A publicly available raw k-space and DICOM dataset of knee images for accelerated MR image reconstruction using machine learning," *Rad. Artif. Intell.*, vol. 2, no. 1, p. e190007, 2020.
- [60] T. Zhang, J. M. Pauly, S. S. Vasanawala, and M. Lustig, "Coil compression for accelerated imaging with cartesian sampling," *Magn. Reson. Med.*, vol. 69, no. 2, pp. 571–582, 2013.
- [61] M. Uecker, P. Lai, M. J. Murphy, P. Virtue, M. Elad, J. M. Pauly, S. S. Vasanawala, and M. Lustig, "Espirit—an eigenvalue approach to autocalibrating parallel mri: where sense meets grappa," *Magn. Reson. Med.*, vol. 71, no. 3, pp. 990–1001, 2014.
- [62] M. Lustig, D. Donoho, and J. M. Pauly, "Sparse mri: The application of compressed sensing for rapid mr imaging," *Magn. Reson. Med.*, vol. 58, no. 6, pp. 1182–1195, 2007.
- [63] J. Leuschner, M. Schmidt, D. O. Bagger, and P. Maass, "Lodopab-ct, a benchmark dataset for low-dose computed tomography reconstruction," *Scientific Data*, vol. 8, no. 1, p. 109, 2021.
- [64] R. Wu, Y. Liu, P. Liang, and Q. Chang, "Only Positive Cases: 5-fold High-order Attention Interaction Model for Skin Segmentation Derived Classification," *arXiv:2311.15625*, 2023.
- [65] E. Zhu, Z. Chen, D. Wang, H. Shi, X. Liu, and L. Wang, "UNetMamba: An Efficient UNet-Like Mamba for Semantic Segmentation of High-Resolution Remote Sensing Images," *IEEE Geosci. Remote Sensing Lett.*, vol. 22, p. 1–5, 2025.
- [66] B. Yaman, S. A. H. Hosseini, S. Moeller, J. Ellermann, K. Uğurbil, and M. Akçakaya, "Self-supervised learning of physics-guided reconstruction neural networks without fully sampled reference data," *Magn. Reson. Med.*, vol. 84, no. 6, pp. 3172–3191, 2020.
- [67] M. Yurt, O. Dalmaz, S. Dar, M. Ozbey, B. Tmaz, K. Oguz, and T. Çukur, "Semi-Supervised Learning of MRI Synthesis Without Fully-Sampled Ground Truths," *IEEE Trans. Med. Imaging*, vol. 41, no. 12, pp. 3895–3906, 2022.
- [68] J. Liu, Y. Sun, C. Eldeniz, W. Gan, H. An, and U. S. Kamilov, "Rare: Image reconstruction using deep priors learned without groundtruth," *IEEE J. Sel. Top. Signal Process.*, vol. 14, no. 6, pp. 1088–1099, 2020.
- [69] M. Ozbey, O. Dalmaz, S. U. H. Dar, H. A. Bedel, S. Ozturk, A. Gungor, and T. Çukur, "Unsupervised medical image translation with adversarial diffusion models," *IEEE Trans. Med. Imaging*, vol. 42, no. 12, pp. 3524–3539, 2023.
- [70] F. Arslan, B. Kabas, O. Dalmaz, M. Ozbey, and T. Çukur, "Self-consistent recursive diffusion bridge for medical image translation," *arXiv:2405.06789*, 2024.
- [71] H. A. Bedel and T. Çukur, "DreaMR: Diffusion-driven counterfactual explanation for functional MRI," *IEEE Trans. Med. Imaging*, 2024.
- [72] C. Cao, Z.-X. Cui, S. Liu, H. Zheng, D. Liang, and Y. Zhu, "High-frequency space diffusion models for accelerated MRI," *arXiv:2208.05481*, 2022.
- [73] M. U. Mirza, O. Dalmaz, H. A. Bedel, G. Elmas, Y. Korkmaz, A. Gungor, S. U. Dar, and T. Çukur, "Learning fourier-constrained diffusion bridges for mri reconstruction," *arXiv:2308.01096*, 2023.
- [74] D. Narnhofer, K. Hammernik, F. Knoll, and T. Pock, "Inverse gans for accelerated mri reconstruction," in *Wavelets and Sparsity XVIII*, vol. 11138. SPIE, 2019, pp. 381–392.
- [75] M. Z. Darestani and R. Heckel, "Accelerated mri with un-trained neural networks," *IEEE Trans. Comput. Imaging*, vol. 7, pp. 724–733, 2021.
- [76] L. Xiang, Y. Chen, W. Chang, Y. Zhan, W. Lin, Q. Wang, and D. Shen, "Deep-learning-based multi-modal fusion for fast MR reconstruction," *IEEE Trans. Biomed. Eng.*, vol. 66, no. 7, pp. 2105–2114, 2019.
- [77] M. Yurt, M. Ozbey, S. U. Dar, B. Tmaz, K. K. Oguz, and T. Çukur, "Progressively volumetrized deep generative models for data-efficient contextual learning of MR image recovery," *Med. Image Anal.*, vol. 78, p. 102429, 2022.
- [78] M. Yurt, S. U. Dar, A. Erdem, E. Erdem, K. K. Oguz, and T. Çukur, "mustGAN: multi-stream Generative Adversarial Networks for MR Image Synthesis," *Med. Image Anal.*, vol. 70, p. 101944, 2021.
- [79] Şaban Öztürk, O. C. Duran, and T. Çukur, "DenoMamba: A fused state-space model for low-dose CT denoising," *arXiv:2409.13094*, 2024.
- [80] G. Luo, N. Zhao, W. Jiang, E. S. Hui, and P. Cao, "Mri reconstruction using deep bayesian estimation," *Magn. Reson. Med.*, vol. 84, no. 4, pp. 2246–2261, 2020.